Journal of Membrane Science 661 (2022) 120923

Contents lists available at ScienceDirect

Journal of Membrane Science

journal homepage: www.elsevier.com/locate/memsci

Rapid macrovoid characterization in membranes prepared via nonsolvent-induced phase separation: A comparison between 2D and 3D techniques

Alexander T. Bridge [a], Matthew S. Santoso [a], Jessica A. Maisano [b], Alexander V. Hillsley [a], Joan F. Brennecke [a], Benny D. Freeman [a,*]

[a] John J. McKetta Jr. Department of Chemical Engineering, The University of Texas at Austin, 200 E. Dean Keeton Street, Austin, TX, 78712, USA
[b] Jackson School of Geosciences, The University of Texas at Austin, C1100, Austin, TX, 78712, USA

ARTICLE INFO

Keywords:
Image segmentation
Asymmetric membranes
Macrovoids
Computed tomography
Electron microscopy

ABSTRACT

Optimizing the performance of asymmetric membranes prepared via nonsolvent-induced phase separation (NIPS) requires a quantitative understanding of how processing variables influence membrane morphology. Presently, the most useful structural quantification techniques require 3D visualization of the membrane structure and are best suited for studies seeking detailed information on small datasets. This study proposes and validates a rapid and accurate technique for quantifying macroporosity (i.e., D_m), a simple descriptor of sublayer macrovoid content in asymmetric membranes. D_m values measured from segmented cross-sectional imaging performed via X-ray computed tomography (XCT) and scanning electron microscopy (SEM) are presented and compared for three asymmetric membranes prepared from commercial polymers. Importantly, analyses of 3D XCT membrane reconstructions reveal that D_m is described by a single, centralized mean, which demonstrates that macrovoid content is spatially homogenous. Thus, D_m can be approximated from limited sampling of the 2D cross-sectional membrane structure via SEM. A proposed 2D SEM sampling method provides D_m estimates within ±6% of corresponding 3D XCT values with 30 independent measurements for the three membranes. Further sensitivity is achieved using complementary descriptors such as macrovoid count density (i.e., C_m). This technique is thus a useful tool for characterizing macroporosity from a broad selection of membrane samples.

1. Introduction

Since the early 1970s, most industrial membranes have been prepared via nonsolvent-induced phase separation (NIPS) [1,2]. The NIPS process consists of metering a homogenous polymer membrane casting solution to a consistent nominal thickness (e.g., 100–250 μm) and immersing the solution into a coagulant (i.e., nonsolvent), which is typically water [2–5]. Upon immersion, the resulting phase separation produces membranes characterized by an asymmetric morphology having a porous sublayer supporting an 'active' skin layer responsible for the target separation (e.g., particle filtration, desalination, gas or vapor separation, etc.) [2,3]. The porous sublayer provides significant mechanical stability, so the skin layer can be made thin (e.g., ~100 nm) to achieve high flux without compromising selectivity [2,3].

In the decades following its widespread adoption for industrial membrane manufacturing, polymeric membrane fabrication research has focused on controlling the NIPS process to generate application-optimized membrane structures. For example, developments in particle filtration membrane fabrication include the use of casting solution or coagulant additives to regulate pore formation on the active layer or within the sublayer during NIPS [3,6]. The introduction of amphiphilic block copolymer self-assembly during membrane formation (i.e., SNIPS) can create an isoporous skin layer [7]. For molecular separations, the incorporation of a transient 'dry' evaporation step prior to the 'wet' NIPS step allows for the preparation of asymmetric membranes with nonporous skin layers [8,9].

Despite success in adapting NIPS to membrane fabrication for various industrial separations, our understanding of morphology evolution during membrane formation remains rather qualitative. For example, sublayer cross-sectional features including pore asymmetry,

* Corresponding author.
E-mail address: freeman@che.utexas.edu (B.D. Freeman).

https://doi.org/10.1016/j.memsci.2022.120923
Received 28 June 2022; Received in revised form 8 August 2022; Accepted 12 August 2022
Available online 17 August 2022

nodules, micropores, and macrovoids are frequently described in membrane formation studies, but they are seldom analyzed quantitatively [3,5,6,10–12]. Macrovoids, often manifested as large, finger-like or teardrop-shaped pores in asymmetric membrane sublayers, are commonly observed in membranes prepared via NIPS. Higher macroporosity (i.e., greater macrovoid size/count) reduces sublayer mass transfer resistance and improves membrane flux, while lower macroporosity favors mechanical integrity at the expense of flux, and, in some cases, selectivity [3,13,14]. Thus, control over sublayer macrovoid size and quantity is important for optimizing an asymmetric membrane for a desired set of process conditions (i.e., pressure ratio, membrane flux, product purity, etc.).

Several theories on the initiation and growth of macrovoids during NIPS have been proposed [3,5,6,10–12,15,16]. Establishing connections between macrovoid formation and these associated theories requires a means of quantitatively representing membrane structure and relating these quantifiers to measurable NIPS parameters (e.g., casting solution polymer concentration or viscosity, polymer molecular weight or polydispersity, casting solution stability, binary component interactions). This concept has previously been explored through the development of segmentation algorithms for imaged asymmetric membranes and subsequent analysis of the segmented images [17–26].

The most accurate segmentation methods for quantifying membrane porous structure are based on high-resolution 3D computed tomography (CT). Remigy et al. were the first to propose a technique for resolving the 3D structure of an asymmetric membrane using synchrotron radiation computed microtomography (SR μCT) [25]. From 3D representations of hollow fiber membranes, the authors quantified porosity and resolved skin layer defects. Viguié et al. improved this technique to isolate sublayer macrovoids and quantify their size, spatial distribution, and shape using X-ray computed tomography (XCT) [26]. Despite CT's effectiveness, high-resolution SR μCT and XCT equipment is not widely available, and high-resolution sample scans (i.e., micron-scale) can take up to several hours. Some sample types must also be mounted and imaged individually. Thus, CT techniques are most useful for detailed analysis of a small group of samples with larger features consistent with the equipment's resolution. Consequently, they have seen limited use in asymmetric membrane characterization.

2D microscopy, namely scanning electron microscopy (SEM), is much more commonly used in membrane studies than CT, due, in part, to the wider availability of SEM equipment [3]. Although SEM can be used only to process exposed (i.e., fractured) 2D membrane cross-sections, it rapidly produces ultra-high resolution (i.e., nanoscale) images, and many SEM instruments can be loaded with batches of ten or more samples at one time.

The widespread availability of SEM has motivated previous studies on the development of segmentation algorithms for processing cross-sectional membrane images. For example, Torras et al. developed an algorithm for characterizing sublayer pore asymmetry, regularity, and count from cross-sectional SEM micrographs of NIPS membranes [23]. The ability to distinguish macrovoids and micropores, with some limitations, was introduced in a subsequent publication [24]. Critiques of both qualitative and quantitative membrane characterization via 2D SEM imaging include its inability to characterize variable 3D structure and the impact of the process of preparing cross-sections for 2D imaging (e.g., freeze fracturing) on membrane structure; both of these factors may compromise accuracy [25,26].

To the best of our knowledge, no existing image processing techniques can both accurately and rapidly quantify structural features (e.g., micropores, macrovoids, pore asymmetry, etc.) in asymmetric membrane samples. In this study, we propose and validate a technique to rapidly and accurately characterize sublayer macrovoid content (i.e., macroporosity or D_m) via cross-sectional SEM imaging. The technique distinguishes and isolates macrovoids from surrounding micropores and quantifies 2D macroporosity from several SEM micrographs captured from the cross-sections of membrane samples. The effectiveness of the 2D SEM approach and the extent of sampling required to faithfully interrogate spatial 3D variations in macroporosity are established via direct comparison to comprehensive 3D structural analyses performed using segmented XCT data. Limitations of D_m as a standalone quantifier of macrovoid content are also explored, and an additional descriptor of normalized cross-sectional macrovoid count (i.e., C_m) is proposed to improve 2D measurement sensitivity.

2. Materials and methods

2.1. Materials

A low cyclic dimer grade of polysulfone (Udel® P3500 MB7 PSf) and a high viscosity grade of poly(amide-imide) (Torlon® 4000T HV) were purchased from Solvay S.A. and used as received. Matrimid® 5218 polyimide and Ultem® 1000 polyetherimide were kindly provided by Air Liquide. Anhydrous *N,N*-dimethylacetamide (99.8%), *N*-methyl-2-pyrrolidone (99.5%), and *N,N*-dimethylformamide (99.8%) were purchased from MilliporeSigma and used as received. A Millipore Milli-Q Advantage A-10 system fed with RO water produced deionized (DI) water at ~23 °C that served as the coagulation medium for membrane fabrication. Methanol (≥99.8%) and *n*-hexane (≥95%) for solvent exchange were purchased from MilliporeSigma and used as received.

2.2. Asymmetric membrane preparation via NIPS

Membrane casting solution preparation was preceded by drying polymer samples under vacuum at 150 °C for 24 h to remove sorbed water. The dried polymer samples were then weighed in 20 mL scintillation vials followed by the addition of the appropriate amount of solvent. Casting solutions were left to stir at elevated temperature (40–70 °C) for at least two days prior to membrane casting.

Once a homogenous mixture was achieved, the casting solutions were poured onto a glass plate and metered to a thickness of 250 μm with a doctor blade. The cast solution was then immediately placed into a coagulation bath containing DI water to undergo NIPS. That is, there was no intentional 'dry step' time used to prepare these membranes [8,9]. All membrane castings were performed at room temperature (~23 °C) and ~50% RH. Each resulting membrane was transferred to a jar of fresh DI water and left to soak overnight to leach out residual solvent. Next, solvent exchange was performed by transferring membranes from water to methanol for 24 h and then to *n*-hexane for 24 h to mitigate pore shrinkage/collapse when drying the membranes. Solvent-exchanged membranes were left to dry in air prior to characterization.

2.3. 2D asymmetric membrane characterization via scanning electron microscopy (SEM)

Membrane cross-sections were prepared via cryo-fracturing in liquid nitrogen (LN2). Square membrane coupons ≥2 cm × 2 cm were soaked in *n*-hexane for 15–30 s to fill the porous sublayer. The soaked membrane coupons were then transferred to an LN2 bath where the imbibed *n*-hexane was allowed to freeze for 15–30 s. The sample was then fractured in the LN2 bath via bending from both ends with a pair of angle-tip forceps. This produced a brittle fracture in the center of the sample and minimized structural distortion in the exposed cross-section.

Mounted cross-sections were sputter-coated with a 40:60 Au/Pt alloy for 90 s and imaged on a Quanta 650 ESEM at 20–30 kV with a spot size of 3.0. For each sample, 10–30 unique micrographs were acquired along two cross-sections to sample a representative cross-section of the membrane area.

2.4. 3D asymmetric membrane characterization via X-ray computed tomography (XCT)

Asymmetric membrane samples were scanned at the University of Texas High-Resolution X-ray CT Facility using the 20× objective on a Zeiss Xradia 620 Versa. The X-ray source was set to 80 kV and 10 W with no filter. 1601 3.5-s projections were acquired over ±180° of rotation with no frame averaging. A source-object distance of 28.5 mm and a detector-object distance of 10.1 mm yielded 1.00-μm resolution. Due to the instrument's approximately micron-scale scan resolution, only membrane samples with large macrovoids (i.e., cross-sectional width generally >10 μm) were suitable for XCT characterization.

3. Results and discussion

This section explores membrane structural characterization and validates the utility of rapid 2D macroporosity quantification via SEM against 3D quantification via XCT. First, the topics of qualitative morphology analysis and image segmentation are discussed for 2D and 3D representations of asymmetric membranes in Sections 3.1 and 3.2. Section 3.3 describes macroporosity calculation from segmented membrane cross-sectional images. Section 3.4 establishes the basis for relating 2D and 3D macroporosity calculations and explores the spatial evolution of macroporosity in segmented 3D XCT scans of three selected asymmetric membranes. Section 3.5 demonstrates the application of rapid 2D macroporosity quantification via SEM for the selected membranes and compares these results to those obtained via 3D XCT.

3.1. Qualitative 2D membrane morphology characterization via SEM

Asymmetric membranes were prepared from Matrimid® 5218 polyimide, Torlon® poly(amide-imide), Udel® polysulfone and Ultem® poly(etherimide), using *N,N*-dimethylacetamide (DMAc), *N,N*-dimethylformamide (DMF), and *N*-methyl-2-pyrrolidone (NMP) as solvents. Casting solution polymer concentrations ranged from 5 to 45 wt %, and deionized water was used as the coagulant (i.e., nonsolvent) in all cases.

2D cross-sectional asymmetric membrane morphology was characterized via SEM. Fig. 1 presents typical cross-sectional SEM images of asymmetric membranes prepared from Matrimid® 5218 polyimide and Torlon® poly(amide-imide) solutions in DMAc, DMF, and NMP. Cross-sections prepared from Udel® polysulfone and Ultem® poly(etherimide) are presented in SI Section S1. Apparent macrovoid content, or macroporosity, varies in the cross-sections depending on polymer-solvent pairing and polymer concentration in the casting solution. In certain cases, these differences are apparent without quantifying membrane morphology. For example, 2D macrovoid size in all membranes often decreases as polymer volume fraction in the casting solution, ϕ_p, is increased. Qualitative comparison generally fails to distinguish samples on the basis of macroporosity, especially when comparing different membrane forming systems. For example, macroporosity is qualitatively indistinguishable between membranes prepared from Torlon®-DMAc and Torlon®-DMF casting solutions when $\phi_p \leq 0.13$. Membranes prepared from Matrimid®-NMP and Torlon®-NMP also appear similarly macroporous when $\phi_p \leq 0.17$.

In most instances where SEM is used to visualize the morphology of asymmetric membranes formed by NIPS, samples are characterized with a single image of the membrane cross-section occupying the entire field of view, as shown in Fig. 1 [6,10,11,27]. Closer inspection of morphology variation in samples with lower sublayer macrovoid content underscores the risk of introducing detection bias with this characterization approach. Fig. 2 shows how qualitative sublayer macroporosity can vary in different regions of a membrane's cross-section.

Considering the images presented in Fig. 2, different interpretations of membrane morphology could arise depending on where an operator chooses to image the samples. For example, one might conclude that, via aqueous NIPS, the Matrimid®-DMF system produces either a nearly macrovoid-free structure based on Fig. 2a, or a significantly macroporous structure based on Fig. 2c. Thus, the accuracy of a qualitative 2D macroporosity estimate depends on how well an image represents the overall membrane structure. This dependence is greatly reduced when multiple images are used to 'sample' the membrane and account for

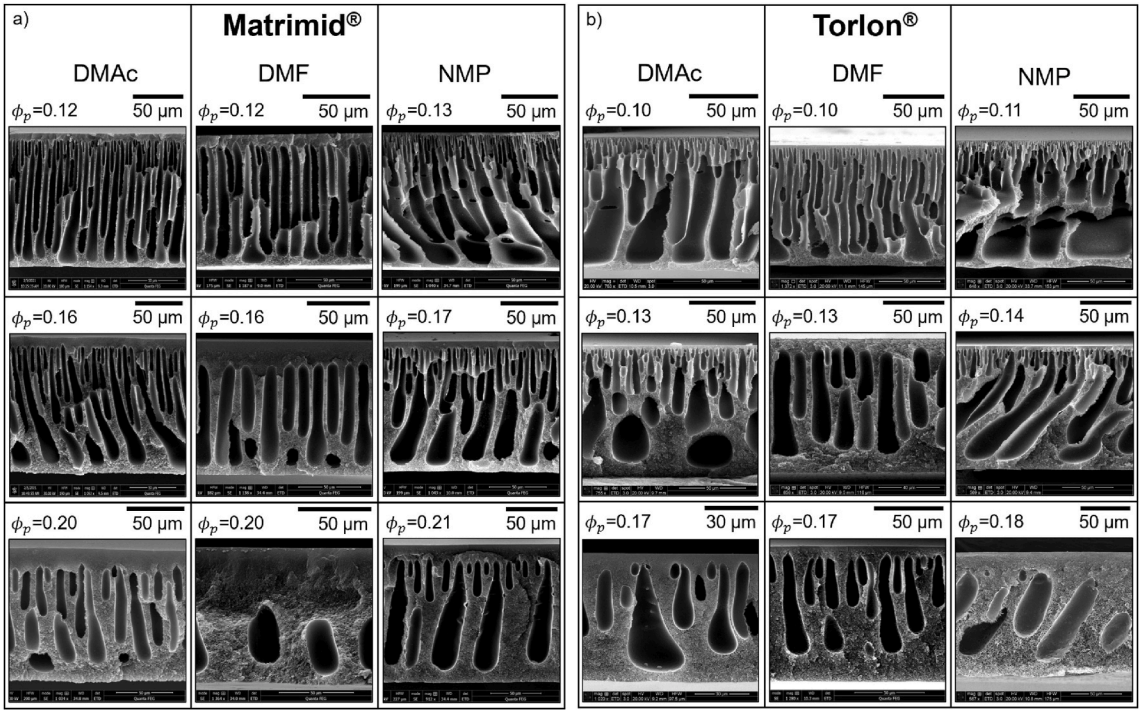

Fig. 1. Selected cross-sectional morphologies of membranes prepared from binary casting solutions containing 15, 20, and 25 wt % (a) Matrimid® 5218 or (b) Torlon® in solvent (DMAc, DMF, or NMP respectively). Polymer volume fractions (ϕ_p) and scale bars are indicated above each SEM micrograph.

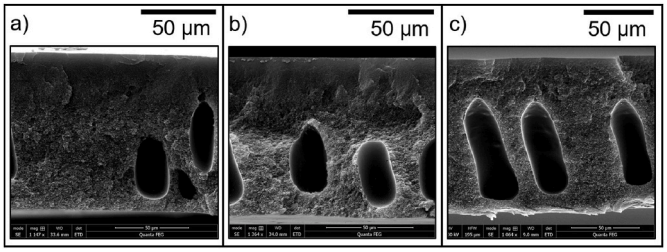

Fig. 2. Cross-sectional morphology of an asymmetric membrane prepared from a solution of 25 wt % Matrimid® (ϕ_p =0.20) in DMF. Images are captured from different regions of the same membrane cross-section showing (a) very few macrovoids, (b) small macrovoids, and (c) large macrovoids.

structural variability. In this study, macroporosity calculations are thus performed on sets of multiple 2D images.

To isolate the 2D structure of macrovoids in membrane cross-sections presented in Figs. 1 and 2, a program was developed to segment SEM micrographs. Image segmentation, as demonstrated in Fig. 3, consisted of cropping all non-cross-sectional features (i.e., visible membrane surfaces, debris, or visible background artifacts) from the original grayscale SEM image (cf. Fig. 3a), binarizing the structure (i.e., converting the grayscale image to a black-and-white colormap via thresholding, cf. Fig. 3b), and eliminating all non-macroporous features (i.e., filling the micropores, cf. Fig. 3c). A detailed description of the segmentation protocol for 2D SEM images is provided in Section S2 of the SI.

More examples of segmented binary representations of membrane structures imaged via SEM are presented in Sections S2 and S10 of the SI (cf. Figs. S6, S7, and S15). The filled binary masks in Fig. 3c, S6, S7, and S15 demonstrate that the proposed SEM segmentation protocol accurately preserves the structure of both large (e.g., >10 μm wide and/or long) and small (e.g., <10 μm wide and/or long) macrovoids, which is a necessary capability for processing the wide variety of macrovoid structures observed in asymmetric membranes prepared via NIPS. The use of segmented images to quantify macroporosity is discussed below, with additional discussion available in Sections S2-S5 of the SI.

3.2. Qualitative 2D & 3D membrane morphology characterization via XCT

XCT scans were performed on three selected asymmetric membranes prepared from 25 wt % Matrimid® in DMF (M1), 25 wt % Matrimid® in DMAc (M2), and 25 wt % Torlon® in DMF (M3). The respective M1-M3 casting solution polymer volume fractions, ϕ_p, were 0.20, 0.20, and 0.17. Scans captured nearly 1000 2D slices, each spaced by ~1 μm, along the samples. Several other samples were scanned, but only these three membranes contained macrovoids large enough to be accurately resolved. The impact of XCT resolution limitations on the analysis of other samples is further elaborated in Section S6 of the SI. Fig. 4 presents representative slices from XCT scans of the three membranes.

Although individual micropores could not be visualized within membrane sublayers due to the micron-scale XCT scan resolution, the 2D size and shape of the larger macrovoids were accurately resolved. The poor resolution of micropores at the XCT scan resolution permitted a more straightforward automated segmentation protocol to binarize the XCT slices. The structure of this program is discussed in SI Section S4, and segmentation examples are presented in SI Sections S6 and S7.

The segmented 2D slices were stacked to create 3D representations of each membrane sample. Truncated 3D structures of the three different samples (i.e., constructed from 200-slice sections of the total segmented XCT scan to highlight 3D structure near the front faces of each membrane) are presented in Fig. 5.

Fig. 5 3D reconstructions provide additional insight into the size, shape, and spacing of macrovoids in each membrane's sublayer. For

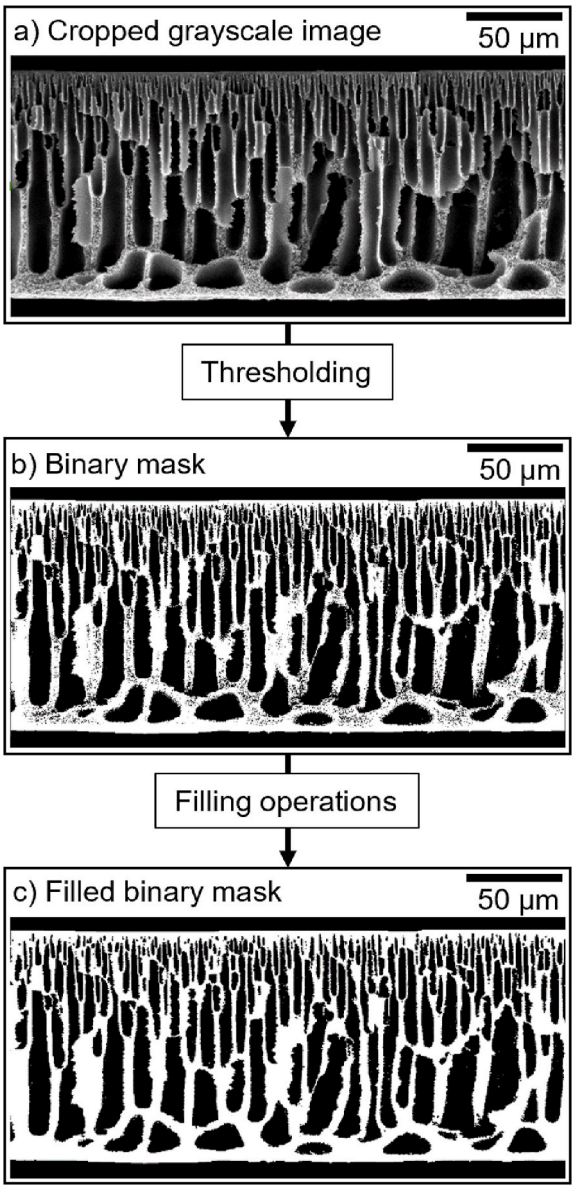

Fig. 3. Segmentation example for a membrane cross-section prepared from 17.5 wt % Ultem® in NMP. The original grayscale SEM micrograph with the metadata bar removed is presented in (a). The resulting unfilled binary structure obtained from adaptive thresholding is presented in (b). The filled binary structure is presented in (c). Scale bars are provided above each image.

example, some round- or teardrop/pear-shaped macrovoids observed near the bottom of 2D M1 cross-sections in Fig. 4a and at the membrane front face in Fig. 5a are found, upon examination of Fig. 5d, to be the ends of longer finger-like macrovoids that began to grow normal (i.e., in the z-direction, cf. Fig. 5) to the 2D image plane (i.e., the x-y plane, cf. Figs. 4 and 5) during membrane formation. Apparent void width also varies normal to the 2D image plane. This pattern is observed for many of the exposed macrovoids in M2 and M3 cross-sections in Fig. 5b and c, which are revealed to be the narrow edges of wider voids centered further within the cross-sections (i.e., further in the z-direction) shown in Fig. 5e and f. These observations are consistent with those in previous studies detailing 3D macrovoid structure [26].

Regardless of the sample, the macrovoid spatial distribution in the x-z plane appears random (i.e., no visible clusters with distinct spacing from other macrovoids in the 3D membrane structure), consistent with previous observations for asymmetric membranes prepared via aqueous

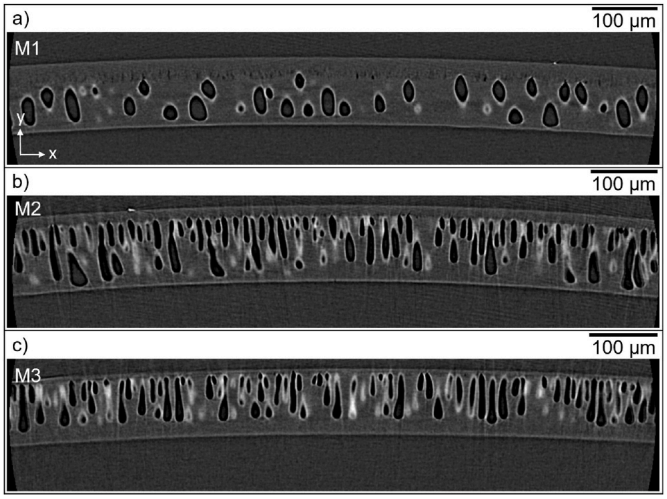

Fig. 4. Representative XCT slices depicting cross-sections membranes prepared from 25 wt % (a) Matrimid® in DMF (M1, $\phi_p = 0.20$), (b) Matrimid® in DMAc (M2, $\phi_p = 0.20$), and (c) Torlon® in DMF (M3, $\phi_p = 0.17$). Scale bars are indicated above each XCT slice. These 2D cross-sections are the front faces of the 3D structures depicted in Fig. 5.

NIPS [26]. Because individual 2D images of membrane cross-sections cannot capture spatial variations in macrovoid structure, as discussed in Section 3.1, corresponding macroporosity calculations will misrepresent true macroporosity values. As more of the membrane cross-section is sampled, the effect of variable macrovoid size and shape on macroporosity can be captured and represented with an average value and a confidence interval, as will be discussed in Sections 3.4 and 3.5.

3.3. 2D macroporosity calculation from individual XCT slices and SEM micrographs

Macroporosity (D_m) is a 2D proxy for the volume fraction (i.e., relative to the volume of the entire membrane structure) occupied by macrovoids in the porous sublayer. The general formula for calculating D_m from a 2D cross-sectional image is defined by Eq. (1):

$$D_m = \frac{A_m}{A_T} \tag{1}$$

where A_m is the cross-sectional surface area occupied by macrovoids within a total membrane cross-section of surface area A_T.

Fig. 6 presents highlighted (i.e., blue) macrovoids overlaid on a grayscale SEM micrograph of an asymmetric membrane prepared from a casting solution of 25 wt % Torlon® in DMAc. Based on Eq. (1), the corresponding 2D macroporosity is calculated from Fig. 6 as:

$$D_m = \frac{Blue\ Area}{Blue\ Area + Orange\ Area}$$

Idealized examples of 2D D_m calculation and further related discussion are available in Sections S2-S5 of the SI. Tests of accurate and equivalent 2D D_m calculation using the SEM and XCT segmentation programs described in this study are provided in SI Section S5.

3.4. 3D macroporosity calculation and analysis from XCT scans

Based on the 2D definition of macroporosity in Eq. (1) and the 3D representations of asymmetric membrane structures presented in Fig. 5, a volumetric representation of macroporosity, $D_{m,V}$, is related to the 2D cross-sectional area occupied by macrovoids relative to the 2D cross-sectional area of the entire membrane structure via Eq. (2):

$$D_{m,V} = \frac{V_m}{V_T} = \frac{\int_0^L A_m(z)dz}{\int_0^L A_T(z)dz} \tag{2}$$

where V_m and V_T are the volumes occupied, respectively, by all macrovoids and the total membrane structure (i.e., microporous region and macrovoids). $A_m(z)$ and $A_T(z)$ represent functions describing the spatial evolution (i.e., along the z-axis) in 2D cross-sectional areas occupied by macrovoids and the total membrane structure in the x-y plane, respectively, and L is the total sample length along the z-axis.

In theory, integrating functions describing cross-sectional area evolution in the z-direction (i.e., $A_m(z)$ and $A_T(z)$) yields volumes occupied by the macrovoids and the total membrane. In practice, macrovoids are discontinuous structures that lack a well-defined and predictable 3D shape, rendering their mathematical representation impractical. Using cross-sectional area data measured across all N slices, equally spaced by a voxel width of Δz, that comprise an XCT scan permits approximation of the definite integrals in Eq. (2) via Riemann sums:

$$D_{m,V} \approx \frac{\sum_{i=1}^{N} A_{m,i}\Delta z}{\sum_{i=1}^{N} A_{T,i}\Delta z} = \frac{\sum_{i=1}^{N} A_{m,i}}{\sum_{i=1}^{N} A_{T,i}} \tag{3}$$

where $A_{T,i}$ and $A_{m,i}$ are the 2D cross-sectional areas occupied by the total membrane structure and macrovoids measured for slice i, respectively. For a fixed field of view, $A_{T,i}$ remains approximately constant across all slices of an XCT scan (see SI Section S8 for more detail), making Eq. (3) $D_{m,V}$ estimate essentially identical to the average of all Eq. (1) slice i 2D $D_{m,i}$ values for the N slices comprising the XCT scan (i.e., $\overline{D_m}$).

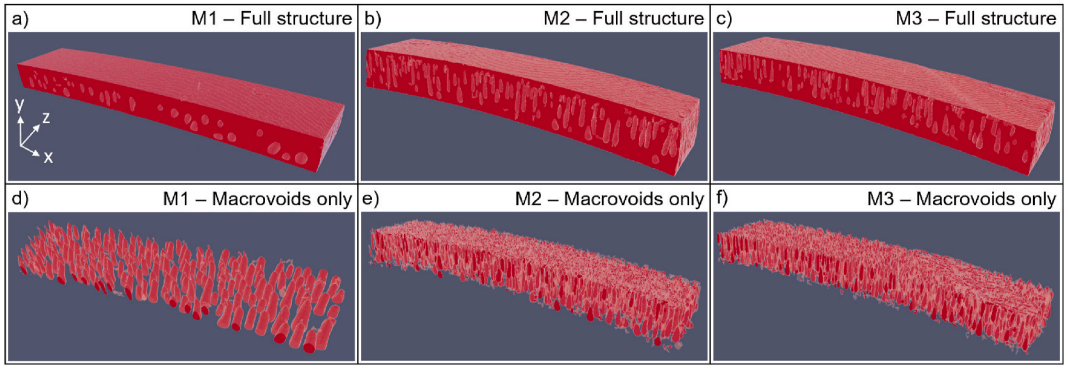

Fig. 5. Segmented 3D XCT reconstructions of membranes prepared from 25 wt % Matrimid® in DMF (M1), 25 wt % Matrimid® in DMAc (M2), and 25 wt % Torlon® in DMF (M3). Full membrane structures are presented in (a–c), and their isolated macrovoid structures are presented in (d–f). 2D scale information for the membranes' front faces in (a–c) (i.e., 2D features visible on the frontal dark red surfaces within the x-y plane) is provided in Fig. 4. (For interpretation of the references to color in this figure legend, the reader is referred to the Web version of this article.)

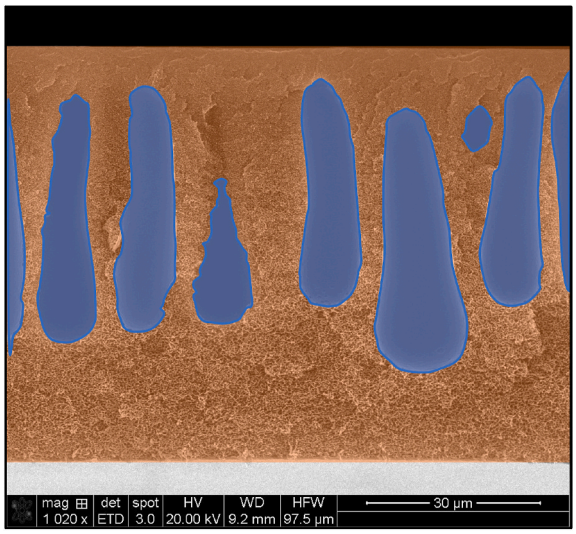

Fig. 6. SEM micrograph of an asymmetric membrane prepared from 25 wt % Torlon® in DMAc. The blue-shaded overlays highlight the 2D structure of macrovoids, and the orange-shaded overlay highlights the microporous sublayer's 2D structure. (For interpretation of the references to color in this figure legend, the reader is referred to the Web version of this article.)

$$\frac{\sum_{i=1}^{N} A_{m,i}}{\sum_{i=1}^{N} A_{T,i}} \approx \frac{1}{N}\sum_{i=1}^{N}\frac{A_{m,i}}{A_{T,i}} = \frac{1}{N}\sum_{i=1}^{N} D_{m,i} = \overline{D_m} \approx D_{m,V} \tag{4}$$

Thus, via Eq. (4), macroporosity can be represented as a cumulative moving average (CMA) that evolves as N, the number of analyzed XCT slices, increases. Fig. 7 presents CMA macroporosity data (i.e., blue curves) for each membrane sample as a function of the number of XCT slices processed. Each membrane's 'true' 3D $D_{m,V}$ value is equated to $\overline{D_m}$ calculated with Eq. (4) from all N slices of the XCT scan. These $\overline{D_m}$ values are indicated in Fig. 7 as horizontal solid lines, in addition to dashed lines that mark ±5% and ±10% deviations from $\overline{D_m}$, to help visualize CMA convergence.

Based on Fig. 7a–c, CMA macroporosity data (i.e., blue curves) rapidly approach their respective $\overline{D_m}$ values as the number of processed XCT slices increase. Inaccuracies beyond ±10% of $\overline{D_m}$ were observed upon calculating CMA macroporosity values from the first few slices from the three XCT scans. Across all XCT slice data, individual slice $D_{m,i}$ deviations from $\overline{D_m}$ can reach values as large as ±30% (i.e., in the case of M1). The deviations from $\overline{D_m}$ observed for M2 and M3 macroporosity data, for both individual slice and CMA values, are lower (i.e., <±20%) than those from M1. This result underscores the challenge of accurately evaluating membrane morphology, qualitatively or quantitatively, from limited cross-sectional imaging data, as discussed in Section 3.1. More sampling may be required for samples with lower macroporosity (i.e., M1) than those of higher macroporosity (i.e., M2 or M3), since low-macroporosity sample $\overline{D_m}$ values are more sensitive to point-to-point variations in macrovoid size, shape, or count.

Initial deviations from $\overline{D_m}$ in Fig. 7a–c CMA data generally decrease to ±10% as the number of processed slices increases from 1 to 10, and ±5% after 30 slices. Further processing of several hundred XCT slices, however, is required to observe CMA macroporosity values that are essentially indistinguishable from $\overline{D_m}$ (i.e., error of ±1%).

Fig. 8 presents histograms of the sorted macroporosity population data (i.e., all individual slice $D_{m,i}$ values) measured from the M1-M3 XCT scans. All three histograms presented in Fig. 8 are unimodal, which suggests that one population of $D_{m,i}$ values exists in the scanned membranes.

Thus, total sublayer macroporosity is well-represented by a single average macroporosity value, $\overline{D_m}$. Fig. 8 histograms confirm morphology expectations for membranes prepared via NIPS with a strong coagulant (i.e., water, as used for the hydrophobic glassy polymers in this study) in which, assuming homogenous polymer distribution in the casting solution, macrovoid growth during phase separation should depend on vertical position relative to the nonsolvent-solution interface rather than on the horizontal (i.e., spatial) position within the nascent membrane [10,11,15,26]. A visual comparison of Fig. 8 $D_{m,i}$ histograms with the scaled normal curve overlays indicates that the population distribution of observed macroporosity values for each membrane is approximately normal. This observation is quantitatively supported by histogram statistics data reported in Table 1 and an analysis of normal quantile plots (cf. Fig. S14 in SI Section S9). Further discussion of $D_{m,i}$ population distributions is available in SI Section S9.

The reported median and modal M1-M3 $D_{m,i}$ values from Fig. 8 macroporosity histograms in Table 1 are all within ±2.5% of their respective means. The $D_{m,i}$ histogram skewness values for all three membranes are small (i.e., <±0.25), so the M1-M3 histograms presented in Fig. 8 are approximately symmetric, which further supports a normally distributed population of macroporosity values. Excess kurtosis values (i.e., relative to a normal distribution) for M1-M3 membranes are all similar and small in magnitude (i.e., <±0.25), indicating that the occurrence of extreme $D_{m,i}$ values (i.e., exceeding ±2 standard deviations from $\overline{D_m}$) follow frequency patterns expected of a normally distributed population. Thus, corroborating data reported in both Fig. S14 and Table 1 indicate that the M1-M3 Fig. 8 $D_{m,i}$ population histograms are normally distributed.

3.5. 2D macroporosity calculation and analysis from SEM imaging

The 3D XCT data analysis in Section 3.4 demonstrates that the M1-M3 $D_{m,i}$ population distributions are unimodal and approximately normal (i.e., symmetrical). Thus, the most probable macroporosity value to be observed is approximately equivalent to the true population mean (i.e., $\overline{D_m}$), and only a single population of macroporosity values exist in NIPS membranes (i.e., no spatial sublayer macroporosity inhomogeneities are observed). The low skewness and excess kurtosis values for these distributions also indicate a low probability of observing outlier $D_{m,i}$ values (i.e., exceeding ±2 standard deviations from $\overline{D_m}$, or <5% of a population that is normally distributed). These findings demonstrate that a sampling approach could be effective in more rapidly estimating the $\overline{D_m}$ value of asymmetric membrane samples.

To estimate $\overline{D_m}$ via sampling, low magnification (500–600x) SEM micrographs were captured along two cross-sections, approximately 2+ cm wide, prepared from M1-M3 membranes. Since macrovoid spatial distribution is random for membranes formed with a strong coagulant (i.e., water in this study) [26], imaging across the width of a few cross-sections captures macrovoid profiles in various positions in the direction normal to the field of view, and it should be a suitable alternative to imaging several unique cross-sections. To test this hypothesis, 30 total micrographs were used to characterize each membrane's 2D macroporosity. Fig. 9 presents representative SEM images of each sample used in this analysis.

As discussed in Section 1, some criticisms of invasive membrane structural analysis via SEM suggest that the technique is compromised by structure distortions introduced upon preparing/fracturing the cross-section for imaging [25,26]. The features present in the SEM micrographs in Fig. 9 and the XCT slices of the same membranes presented in Fig. 4, however, are qualitatively consistent. This observation, paired with quantitative agreement in cross-sectional thickness (i.e., samples M1-M3, respectively, are approximately 103 ± 6, 115 ± 5, and 97 ± 1 µm thick in Figs. 4 and 9) verifies that negligible structural distortion occurred via the freeze fracturing procedure used in this study. The 30 M1-M3 SEM cross-sectional images were segmented using the program described in Section S2 of the SI. More detail on SEM micrograph

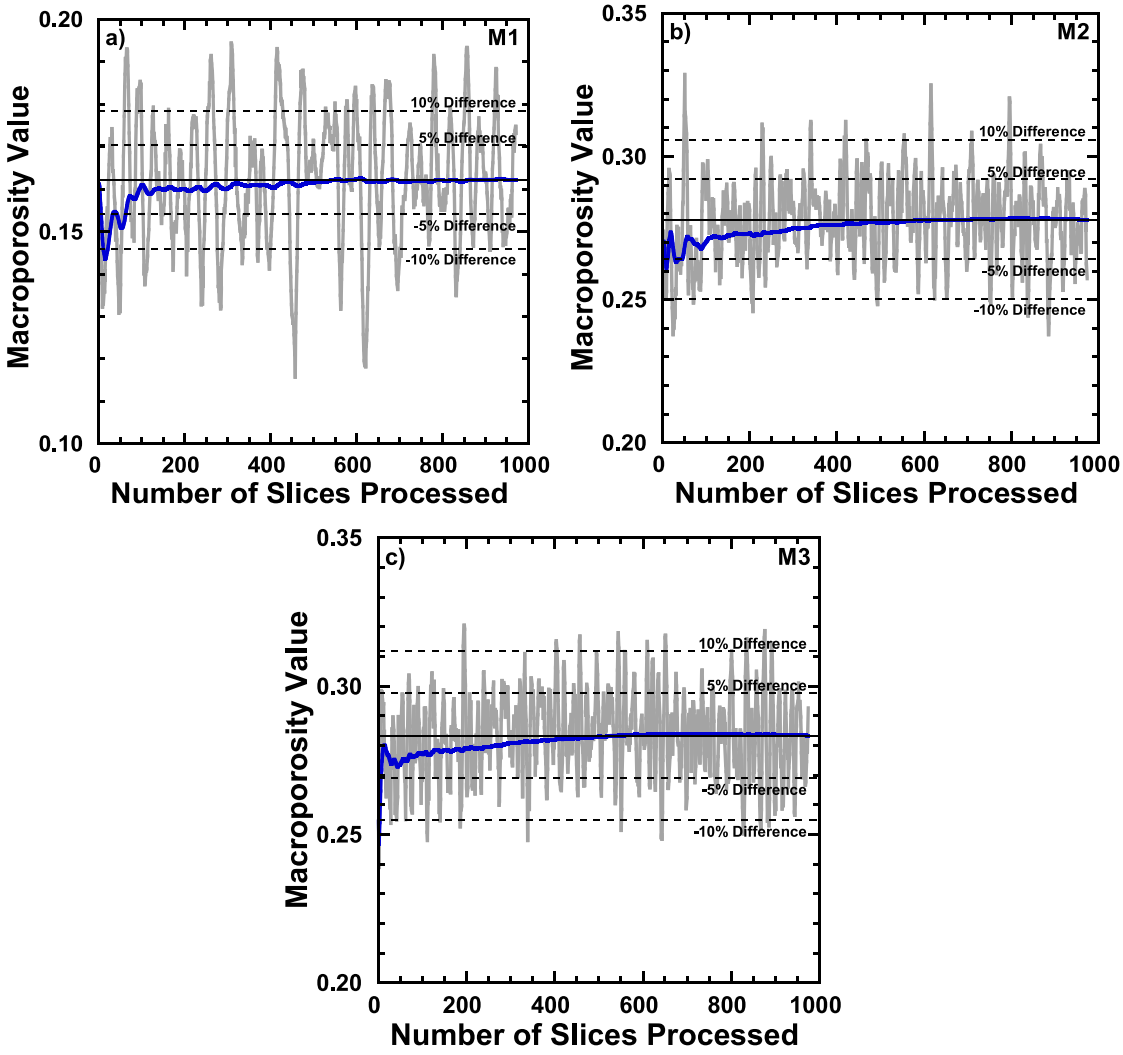

Fig. 7. Relationship between Eq. (4) cumulative moving average (CMA) macroporosity values and the number of slices processed from a continuous XCT scan. Data is shown for scans of membranes prepared from (a) 25 wt % Matrimid® in DMF (M1), (b) 25 wt % Matrimid® in DMAc (M2), and (c) 25 wt % Torlon® in DMF (M3). CMA macroporosity data (blue) calculated with Eq. (4) is superimposed over $D_{m,i}$ values calculated via Eq. (1) for each XCT slice i (gray). Percent differences of ±5 and ± 10 from the mean macroporosity value for the entire XCT scan (i.e., $\overline{D_m}$, indicated with a solid horizontal line) are plotted as horizontal dashed lines. (For interpretation of the references to color in this figure legend, the reader is referred to the Web version of this article.)

segmentation is provided in Sections S2 and S10 of the SI. Fig. 10 presents average macroporosity values (i.e., $\overline{D_m}$) calculated from the segmented micrographs via Eq. (4) in comparison with $\overline{D_m}$ values determined from XCT scans of the same membranes in Section 3.4.

Based on the results in Fig. 10, the 2D SEM $\overline{D_m}$ estimates using 30 discrete micrographs for all three membranes are in good quantitative agreement with the 'true' $\overline{D_m}$ values obtained from 3D XCT scans (i.e., within ±6%). The 2D SEM $\overline{D_m}$ errors are quantitatively consistent with the CMA errors calculated from the first 30 XCT slices in Fig. 7 as discussed in Section 3.4, further demonstrating the accuracy of the proposed sampling technique. The larger 95% confidence interval observed for the M1 SEM analysis underscores the importance of high amounts of 2D sampling in low (i.e., $\overline{D_m} < 0.2$) macroporosity samples to obtain accurate $\overline{D_m}$ values.

A concern with using D_m as a standalone sublayer morphology descriptor is the risk of poor discrimination between membranes that exhibit similar $\overline{D_m}$ values, because macroporosity describes only fractional void space without considering macrovoid size, shape, or count. This challenge is at least partially addressed by reporting values for macrovoid count density, or C_m, expressed as the number of observed macrovoids per unit cross-sectional area, for membrane cross-sections. As with D_m, the random spatial distribution of macrovoids throughout asymmetric membranes prepared with a strong coagulant enables a sampling approach for estimating C_m [26]. Using available scale information from the SEM micrograph's metadata, C_m is calculated from a 2D membrane cross-section via Eq. (5):

$$C_m = \frac{Cross\text{-}Sectional\ Macrovoid\ Count}{Cross\text{-}Sectional\ Membrane\ Area} \tag{5}$$

To exemplify the utility of C_m as an added morphology descriptor, Fig. 11 presents cross-sectional SEM images of two highly macroporous asymmetric membranes prepared from 20 wt % Ultem® in DMAc (Fig. 11a) and NMP (Fig. 11b) casting solutions. Although these structures appear qualitatively distinct (i.e., there are fewer but consistently longer macrovoids in Fig. 11a cross-section compared with Fig. 11b), their $\overline{D_m}$ values are statistically identical after processing 10 SEM micrographs (i.e., their confidence intervals overlap), as shown in Table 2.

Thus, the membranes shown in Fig. 11 cannot be quantitatively differentiated based on macroporosity alone, despite their qualitatively distinct morphologies. By measuring and reporting their average C_m

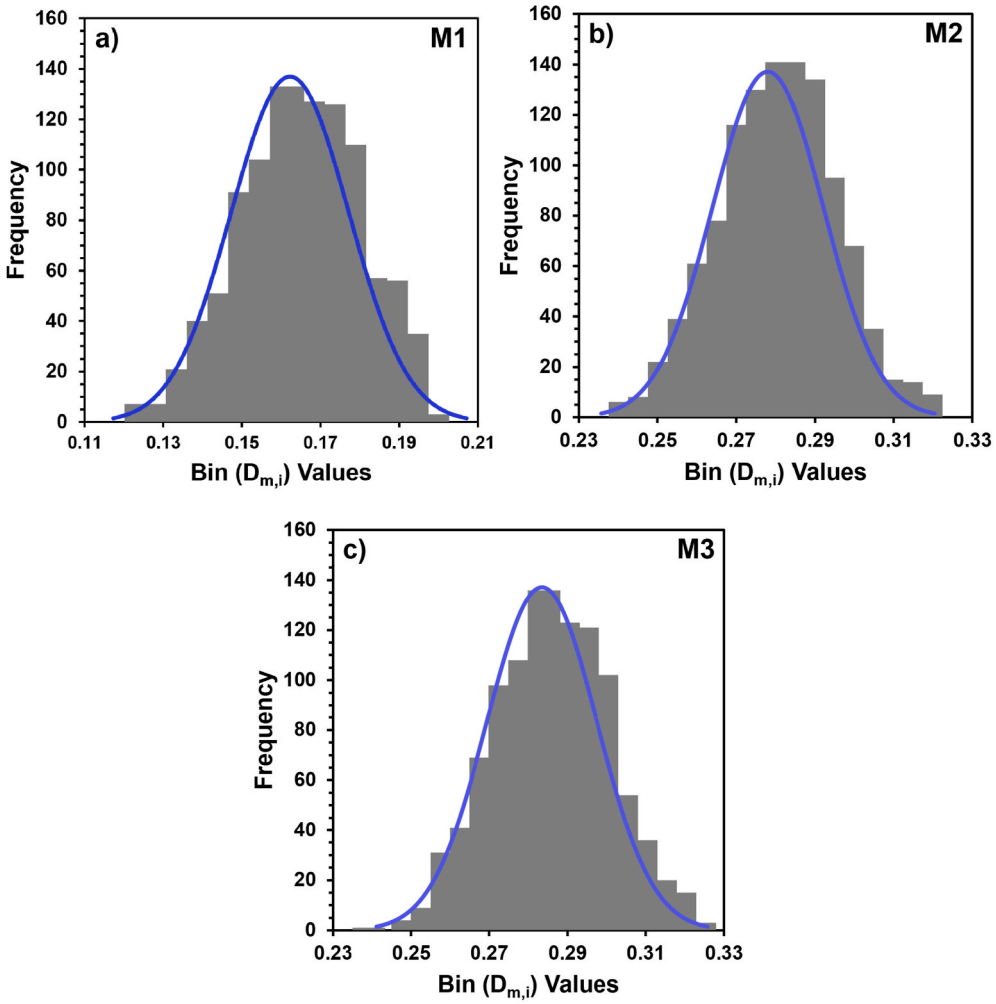

Fig. 8. Histograms of individual slice $D_{m,i}$ values observed from all N slices in 3D XCT scans of membranes prepared from (a) 25 wt % Matrimid® in DMF (M1), (b) 25 wt % Matrimid® in DMAc (M2), and (c) 25 wt % Torlon® in DMF (M3). Normal curve overlays (blue), which are scaled to match the areas under the respective histograms, are included to guide the eye. (For interpretation of the references to color in this figure legend, the reader is referred to the Web version of this article.)

Table 1
Skewness and tailedness statistics for Fig. 8 XCT $D_{m,i}$ population histograms. Data shown for membranes prepared from 25 wt % Matrimid® in DMF (M1), 25 wt % Matrimid® in DMAc (M2), and 25 wt % Torlon® in DMF (M3).

Sample	Mean $D_{m,i}$ value ($\overline{D_m}$)	Median $D_{m,i}$ value	Modal $D_{m,i}$ value*	Skewness	Excess Kurtosis
M1	0.162	0.162	0.160	−0.228	−0.255
M2	0.278	0.279	0.284	0.032	0.199
M3	0.283	0.283	0.284	−0.010	−0.277

*Most frequently occurring D_m value to 3 significant digits.

values (i.e., $\overline{C_m}$), however, this qualitative difference is instead captured with respect to macrovoid quantity, as shown in Table 2.

Based on Table 2 $\overline{D_m}$ and $\overline{C_m}$ data, the apparent difference in morphology between the membranes presented in Fig. 11 is caused primarily by a difference in macrovoid count. Although the membrane prepared from 20 wt % Ultem® in NMP has over two times more macrovoids per unit area than the membrane prepared from 20 wt % Ultem® in DMAc, many of the Ultem®/NMP membrane's macrovoids are clearly smaller (i.e., narrower and shorter) and less uniformly packed than those of the Ultem®/DMAc membrane (cf. Fig. 11). This tradeoff between macrovoid count and packing efficiency contributes to the similar macroporosity values reported in Table 2, thus necessitating the analysis of both $\overline{D_m}$ and $\overline{C_m}$ data to quantitatively distinguish the structures in Fig. 11. A more comprehensive description of macrovoid count density measurement, including a comparison of M2 and M3 membranes using both D_m and C_m data, is provided in SI Section S11.

As discussed previously, the morphology descriptors proposed in this study are intended for rapid characterization of large sample groups. Thus, to contextualize their effectiveness, application of 2D SEM D_m and C_m characterization to a larger group of samples prepared from Ultem® is presented and discussed in SI Section S12. A subsequent publication exploring connections between the quantitative morphology descriptors discussed here and commonly measured parameters (e.g., casting solution viscosity, casting solution polymer concentration, casting solution thermodynamic stability, binary thermodynamic interaction parameters, etc.) for NIPS membrane formation for all four polymers mentioned throughout this manuscript (i.e., Matrimid®, Torlon®, PSf, and Ultem®) is in preparation.

4. Conclusions

In this study, a 2D sampling approach based on SEM is proposed to rapidly characterize asymmetric membrane macroporosity (i.e., D_m value). The first part of this study sought to characterize spatial variations (i.e., in the direction normal to 2D cross-sections) in sublayer macroporosity using XCT scans over large membrane areas. This analysis revealed that sublayer macroporosity varies randomly about a

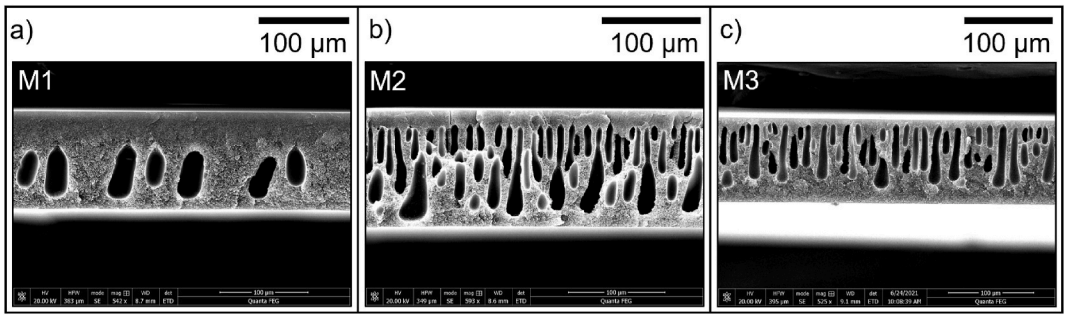

Fig. 9. Representative cross-sectional SEM micrographs of (a) 25 wt % Matrimid® in DMF (M1), (b) 25 wt % Matrimid® in DMAc (M2), and (c) 25 wt % Torlon® in DMF (M3) used for 2D $\overline{D_m}$ calculation.

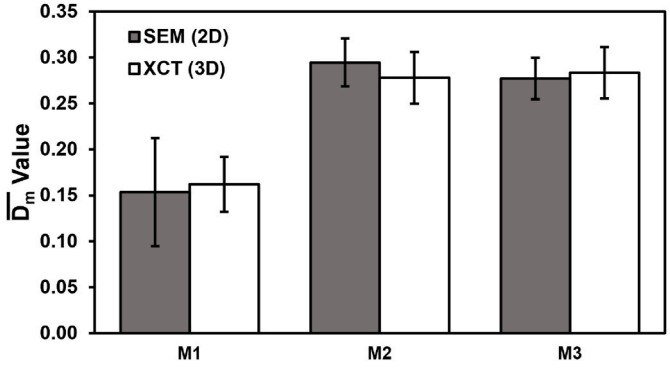

Fig. 10. Comparison between average macroporosity values (i.e., $\overline{D_m}$) calculated with Eq. (4) from segmented SEM and XCT images of membranes prepared from 25 wt % Matrimid® in DMF (M1), 25 wt % Matrimid® in DMAc (M2), and 25 wt % Torlon® in DMF (M3). Error bars represent 95% confidence intervals obtained from D_m population data (i.e., 30 discrete micrographs via SEM or ~1000 continuous slices via XCT).

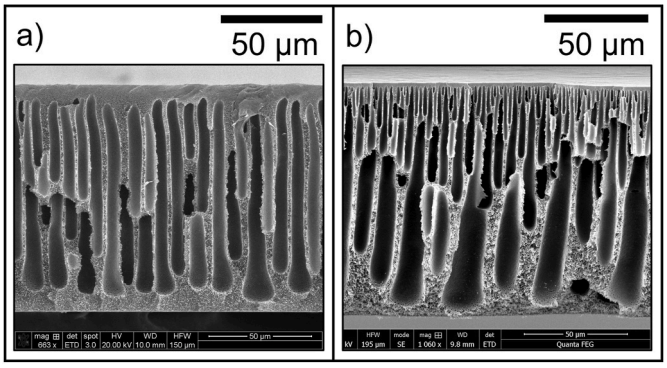

Fig. 11. Representative cross-sectional SEM images of asymmetric membranes prepared from (a) 20 wt % Ultem® in DMAc and (b) 20 wt % Ultem® in NMP.

Table 2
$\overline{D_m}$ and $\overline{C_m}$ data calculated from 10 discrete segmented SEM micrographs of membranes prepared from casting solutions of 20 wt % Ultem® in DMAc and NMP.

Sample	$\overline{D_m}$	$\overline{C_m}$, Macrovoid count density (voids/μm^2) $\times 10^{-4}$
20 wt % Ultem® in DMAc	0.557 ± 0.031	21.6 ± 2.0
20 wt % Ultem® in NMP	0.550 ± 0.020	69.6 ± 3.9

central mean value, which demonstrates that this quantity has no dependence on spatial position in the membrane. This conclusion was supported by an analysis of macroporosity population histograms measured from segmented XCT scan data, which showed that the distributions were unimodal and approximately normal for the three membranes. These findings established the validity of sampling to estimate macroporosity more rapidly (i.e., relative to continuous CT scans) in membranes prepared via NIPS. XCT macroporosity measurements, which were treated as representations of 'true' membrane macroporosity, were then compared to macroporosity sampling estimates from segmented SEM micrographs. This analysis revealed that the proposed SEM sampling approach is accurate for quantifying macroporosity (i.e., within ±6% of the XCT value). Thus, by sampling membrane cross-sectional morphology, sublayer macrovoid size can be effectively compared between asymmetric membrane forming systems in large studies concerned with quantitatively testing the generality of NIPS membrane formation theory. One shortcoming of 2D characterization is the loss of 3D information on macrovoid size, shape, and count. Using additional quantifiers, such as macrovoid count density (i.e., C_m), to complement this technique improves quantitative discrimination between membranes exhibiting similar macroporosity.

Author contributions

Alexander T. Bridge: Conceptualization, methodology, validation, software, formal analysis, investigation, data curation, visualization, writing – original draft, writing – review & editing, project administration. **Matthew S. Santoso:** Software, methodology, formal analysis, data curation, validation, writing – original draft, writing – review & editing. **Jessica A. Maisano:** Formal analysis, investigation, writing – original draft, writing – review & editing. **Alexander V. Hillsley:** Software, methodology, writing – review & editing. **Joan F. Brennecke:** Writing – review & editing, supervision, project administration, funding acquisition. **Benny D. Freeman:** Resources, writing – review & editing, supervision, project administration, funding acquisition.

Declaration of competing interest

The authors declare that they have no known competing financial interests or personal relationships that could have appeared to influence the work reported in this paper.

Data availability

Data will be made available on request.

Acknowledgements and funding sources

The authors thank Prof. Michael Baldea for providing useful discussion about image processing strategies and the technique proposed in

this study. The authors also thank Dave Edey for assistance with ORS Dragonfly software. This paper is based upon work supported in part by the National Science Foundation (NSF) under Cooperative Agreement No. EEC-1647722 (A T B., M.S.S., J.F.B., and B.D.F.). Any opinions, findings, and conclusions or recommendations expressed in this material are those of the authors and do not necessarily reflect the views of the NSF. XCT imaging and associated analysis were supported as part of the Center for Materials for Water and Energy Systems, an Energy Frontier Research Center funded by the U.S. Department of Energy, Office of Science, Basic Energy Sciences under Award #DE-SC0019272.

Appendix A. Supplementary data

Supplementary data to this article can be found online at https://doi.org/10.1016/j.memsci.2022.120923.

References

[1] S. Loeb, S. Sourirajan, Sea water demineralization by means of an osmotic membrane, Saline Water Conversion—II 38 (1963) 117–132, https://doi.org/10.1021/ba-1963-0038.
[2] R.W. Baker, Membrane Technology and Applications, third ed., John Wiley & Sons, Chichester, West Sussex ; Hoboken, 2012.
[3] G.R. Guillen, Y. Pan, M. Li, E.M.V. Hoek, Preparation and characterization of membranes formed by nonsolvent induced phase separation: a review, Ind. Eng. Chem. Res. 50 (2011) 3798–3817, https://doi.org/10.1021/ie101928r.
[4] A.J. Reuvers, C.A. Smolders, Formation of membranes by means of immersion precipitation. Part II. The mechanism of formation of membranes prepared from the system cellulose acetate-acetone-water, J. Membr. Sci. 34 (1987) 67–86, https://doi.org/10.1016/S0376-7388(00)80021-6.
[5] C.A. Smolders, A.J. Reuvers, R.M. Boom, I.M. Wienk, Microstructures in phase-inversion membranes. Part 1. Formation of macrovoids, J. Membr. Sci. 73 (1992) 259–275, https://doi.org/10.1016/0376-7388(92)80134-6.
[6] D.-M. Wang, A. Venault, J.-Y. Lai, Fundamentals of nonsolvent-induced phase separation, in: Hollow Fiber Membranes: Fabrication and Applications, Elsevier, 2021, pp. 13–56, https://doi.org/10.1016/B978-0-12-821876-1.00009-3.
[7] M. Müller, V. Abetz, Nonequilibrium processes in polymer membrane formation: theory and experiment, Chem. Rev. 121 (2021) 14189–14231, https://doi.org/10.1021/acs.chemrev.1c00029.
[8] I. Pinnau, Skin Formation of Integral-Asymmetric Gas Separation Membranes Made by Dry/wet Phase Inversion, Ph.D. Dissertation, The University of Texas at Austin, 1991.
[9] S.C. Pesek, W.J. Koros, Aqueous quenched asymmetric polysulfone membranes prepared by dry/wet phase separation, J. Membr. Sci. 81 (1993) 71–88, https://doi.org/10.1016/0376-7388(93)85032-R.
[10] G.R. Guillen, G.Z. Ramon, H.P. Kavehpour, R.B. Kaner, E.M.V. Hoek, Direct microscopic observation of membrane formation by nonsolvent induced phase separation, J. Membr. Sci. 431 (2013) 212–220, https://doi.org/10.1016/j.memsci.2012.12.031.
[11] H. Strathmann, K. Kock, P. Amar, R.W. Baker, The formation mechanism of asymmetric membranes, Desalination 16 (1975) 179–203, https://doi.org/10.1016/S0011-9164(00)82092-5.
[12] R.M. Boom, I.M. Wienk, Th van den Boomgaard, C.A. Smolders, Microstructures in phase inversion membranes. Part 2. The role of a polymeric additive, J. Membr. Sci. 73 (1992) 277–292, https://doi.org/10.1016/0376-7388(92)80135-7.
[13] I. Pinnau, W.J. Koros, Relationship between substructure resistance and gas separation properties of defect-free integrally skinned asymmetric membranes, Ind. Eng. Chem. Res. 30 (1991) 1837–1840, https://doi.org/10.1021/ie00056a024.
[14] A.T. Bridge, B.J. Pedretti, J.F. Brennecke, B.D. Freeman, Preparation of defect-free asymmetric gas separation membranes with dihydrolevoglucosenone (CyreneTM) as a greener polar aprotic solvent, J. Membr. Sci. 644 (2022), https://doi.org/10.1016/j.memsci.2021.120173.
[15] S.A. McKelvey, W.J. Koros, Phase separation, vitrification, and the manifestation of macrovoids in polymeric asymmetric membranes, J. Membr. Sci. 112 (1996) 29–39, https://doi.org/10.1016/0376-7388(95)00197-2.
[16] D.R. Tree, L.F. Dos Santos, C.B. Wilson, T.R. Scott, J.U. Garcia, G.H. Fredrickson, Mass-transfer driven spinodal decomposition in a ternary polymer solution, Soft Matter 15 (2019) 4614–4628, https://doi.org/10.1039/C9SM00355J.
[17] K.-L. Tung, K.-S. Chang, T.-T. Wu, N.-J. Lin, K.-R. Lee, J.-Y. Lai, Recent advances in the characterization of membrane morphology, Current Opinion in Chemical Engineering 4 (2014) 121–127, https://doi.org/10.1016/j.coche.2014.03.002.
[18] K.S. Choudhari, P. Jidesh, P. Sudheendra, S.D. Kulkarni, Quantification and morphology studies of nanoporous alumina membranes: a new algorithm for digital image processing, Microsc. Microanal. 19 (2013) 1061–1072, https://doi.org/10.1017/S1431927613001542.
[19] L. Zeman, L. Denault, Characterization of microfiltration membranes by image analysis of electron micrographs. Part I. Method development, J. Membr. Sci. 71 (1992) 221–231, https://doi.org/10.1016/0376-7388(92)80207-Z.
[20] R. Ziel, A. Haus, A. Tulke, Quantification of the pore size distribution (porosity profiles) in microfiltration membranes by SEM, TEM and computer image analysis, J. Membr. Sci. 323 (2008) 241–246, https://doi.org/10.1016/j.memsci.2008.05.057.
[21] Q. Wu, B. Wu, Study of membrane morphology by image analysis of electron micrographs, J. Membr. Sci. 105 (1995) 113–120, https://doi.org/10.1016/0376-7388(95)00055-H.
[22] H. Vivier, M.-N. Pons, J.-F. Portala, Study of microporous membrane structure by image analysis, J. Membr. Sci. 46 (1989) 81–91, https://doi.org/10.1016/S0376-7388(00)81172-2.
[23] C. Torras, R. Garcia-Valls, Quantification of membrane morphology by interpretation of scanning electron microscopy images, J. Membr. Sci. 233 (2004) 119–127, https://doi.org/10.1016/j.memsci.2003.12.016.
[24] C. Torras, D. Puig, M. Ángel García, A new method to quantify parameters of membrane morphology from electron microscopy micrographs by texture recognition, Chem. Eng. Sci. 66 (2011) 4582–4594, https://doi.org/10.1016/j.ces.2011.06.013.
[25] J.C. Remigy, M. Meireles, X. Thibault, Morphological characterization of a polymeric microfiltration membrane by synchrotron radiation computed microtomography, J. Membr. Sci. 305 (2007) 27–35, https://doi.org/10.1016/j.memsci.2007.06.059.
[26] J. Viguié, T. Savart, P. Duru, J.-C. Rouch, J.-C. Remigy, Characterisation of 3D porous macrostructure of hollow fibre membranes using X-ray tomography—effects of some spinning process conditions, J. Membr. Sci. 435 (2013) 11–20, https://doi.org/10.1016/j.memsci.2013.01.062.
[27] P. van de Witte, P.J. Dijkstra, J.W.A. van den Berg, J. Feijen, Phase separation processes in polymer solutions in relation to membrane formation, J. Membr. Sci. 117 (1996) 1–31, https://doi.org/10.1016/0376-7388(96)00088-9.